Numerical solution of the time-dependent Maxwell's equations for random dielectric media

W. Harshawardhan, Q. Su, and R. Grobe
Intense Laser Physics Theory Unit and Department of Physics, Illinois State University, Normal, Illinois 61790-4560
(Received 2 March 2000)

We discuss how a spectral-domain method in combination with a split-operator technique can be used to calculate exact solutions of the time-dependent Maxwell's equations. We apply this technique to study the tunneling signal of an evanescent wave occurring due to frustrated total internal reflection and the propagation of a light pulse through an inhomogeneous medium consisting of multiple random scatterers.

PACS number(s): 41.20.Jb, 42.25.Dd, 42.25.Bs

I. INTRODUCTION

Modeling of temporal evolution of light in highly scattering media has potential applications in a wide range of fields, such as medical imaging and therapy, radar detection, astronomy, electronic technology, photonic devices, and so on. In recent times, there has been an explosion of interest in such modeling due to the development of solution techniques for partial differential equations (PDE's) as well as the availability of large-scale computational resources. In a complex scattering medium, classical Monte Carlo simulations are sufficient to obtain diffusion effects as confirmed by experiments [1–3]. Other classes of experimental data suggest the importance of phase information which is lacking in the above approach. Dominant features at the near field arise due to the interplay of phases, which calls for the exact solution of the Maxwell's equations beyond the Boltzmann equation. The time-domain PDE Maxwell's equations solvers provide a powerful tool to understand the light-matter interaction at submicron resolution and with the capability of temporal finesse of the order of subpicoseconds.

Some of the most widely used methods for simulating transient electromagnetic wave propagation are the finite-difference-time-domain (FDTD) methods. These methods involve approximating the derivatives in the Maxwell's equations by finite differences. Yee [4] described the first space grid-based time integration. In the Yee algorithm, the electric- and magnetic-field components are located at different positions in a *staggered* grid. This algorithm has a second-order accuracy in both space and time. To increase accuracy in the FDTD methods, typically one would have to increase the grid density and/or use higher-order differencing. Since this early demonstration, the FDTD technique has matured and has been adopted by researchers in diverse fields. Taflove coined the acronym FDTD and demonstrated the first three-dimensional grid-based computational model of electromagnetic wave absorption in complex, inhomogeneous biological tissues [5]. References [6] and [7] contain detailed references and reviews on the FDTD methods. A nice survey of FDTD literature that includes almost 500 references has been provided by Shlager and Schneider [8].

In this paper, we introduce another technique which exploits the simplicity of evolution of the field components in the spectral domain to obtain the time-dependent solutions of the Maxwell's equations. In this method, efficient fast Fourier transforms (FFT) are used to represent the spatial derivatives. We point out a few advantages of the spectral-domain technique over the FDTD methods. The FDTD method typically requires at least 10–20 grid points per wavelength, whereas the spectral-domain method can be applied with fewer grid points, as permitted by the Nyquist sampling theorem. Spectral methods can be efficiently implemented on parallel computers. Moreover, the electric- and magnetic-field components are located at the same spatial location. Recent studies [10] have claimed that the spectral-domain technique in comparison with the FDTD method can require less computation time and associated memory.

On the other hand, the proposed algorithm also has several drawbacks. In its present form, dispersive effects due to frequency-dependent materials are not taken into account in this algorithm, while other FDTD models do [11]. Although an integration in frequency space requires fewer grid points than a method based on the finite-difference approximation to the first- and second-order derivatives for comparable accuracy, the required Fourier transformation is slower than the associated tridiagonal matrix manipulations in the FD models. The present model could be advantageous for computational situations, in which memory constraints require a restricted number of grid points, and CPU time is of no concern. Another disadvantage of the split-operator FFT scheme is the fact that a change from Cartesian to more general nonuniform grid coordinates is nontrivial. An additional disadvantage of the spectral-domain technique is the wrap-around effect, which we have overcome by the choice of appropriate boundary conditions; the details are provided in Secs. II B and II C. The past decade has shown that in atomic ionization physics, numerical wave-function solutions to the time-dependent Schrödinger and Dirac equations can be calculated from FDTD as well as split-operator FFT methods with comparable computational efficiency.

In Sec. II, we describe the details of the numerical method, how the electromagnetic radiation pulse is evolved in space and time, and how the initial and boundary values are incorporated on the spatiotemporal grid. In Sec. III, we test our method for simple geometries for which analytical solutions are available. Finally, we give an example of a radiation pulse interacting with an inhomogeneous medium comprised of random dielectric scatterers. We finish this paper with a short conclusion and an outlook on future work.

II. NUMERICAL ALGORITHM

A. The temporal and spatial evolution

We describe in this section the details of the numerical algorithm used to obtain the solution of the Maxwell's equa-

tions. A combination of the spectral-domain method and the split-operator technique is used to calculate the evolution of the electromagnetic fields in inhomogeneous media. In the absence of any free charges and currents, the electromagnetic fields satisfy the following Maxwell's equations (in SI units):

$$\vec{\nabla}\cdot\epsilon(\vec{r})\vec{E}=0, \tag{2.1}$$

$$\vec{\nabla}\cdot\vec{B}=0, \tag{2.2}$$

$$\frac{\partial\vec{E}}{\partial t}=\frac{c^2}{\epsilon(\vec{r})}\vec{\nabla}\times\vec{B}, \tag{2.3}$$

$$\frac{\partial\vec{B}}{\partial t}=-\vec{\nabla}\times\vec{E}, \tag{2.4}$$

where $\vec{E}$ and $\vec{B}$ are the electric and magnetic fields, respectively. The velocity of light in vacuum is c. The relative permeability μ/μ_o is assumed to be unity. The relative dielectric permittivity $\epsilon(\vec{r})$ characterizes the medium and could vary arbitrarily in space depending on the choice of the material configuration. It is clear that Eq. (2.3) can describe only those situations for which the dielectric constant $\epsilon(\vec{r})$ depends weakly on the frequency of the light. In other words, we require the index of refraction $\sqrt{\epsilon(\vec{r})}$ to vary on a frequency scale larger than the spectral width of the
laser pulse. Note that this problem has been overcome in FDTD methods as described, e.g., in Ref. [11]. The spatial variables (x,y,z) and the time (t) are discretized into N_x, N_y, and N_z space points and N_t time steps. The respective step sizes are Δx, Δy, Δz, and Δt. The fields are numerically represented as a vector in Cartesian coordinates $(\vec{E},\vec{B})=(E_x,E_y,E_z,B_x,B_y,B_z)$. The use of these coordinates can greatly simplify the study of dynamics with symmetries such that the spatial dimensions can be reduced. For the situations discussed below, we used a two-dimensional grid with at most $N_y=N_z=1024$ spatial points and roughly $N_t=5000$ time intervals. For this choice of parameters, the equivalent three-dimensional system would be a medium with infinite extension along the x direction.

This time evolution for the state vector $(\vec{E},\vec{B})$ according to Eqs. (2.3) and (2.4) is connected with two differential operators $H^v(\vec{\nabla})$ and $H^m(\vec{\nabla},\vec{r})$, the first of which generates the evolution of the field through the vacuum and the second one contains the effect of the medium. They are explicitly written as

$$H^v(\vec{\nabla})\equiv\begin{pmatrix}0 & \vec{\nabla}\times\\ -\vec{\nabla}\times & 0\end{pmatrix}, \tag{2.5}$$

$$H^m(\vec{\nabla},\vec{r})\equiv\left[\frac{c^2}{\epsilon(\vec{r})}-1\right]\begin{pmatrix}0 & \vec{\nabla}\times\\ 0 & 0\end{pmatrix}. \tag{2.6}$$

The time evolution for a single time step Δt is given by

$$\begin{pmatrix}\vec{E}(\vec{r},t+\Delta t)\\ \vec{B}(\vec{r},t+\Delta t)\end{pmatrix}=\exp\{\Delta t[H^v(\vec{\nabla})+H^m(\vec{\nabla},\vec{r})]\}\begin{pmatrix}\vec{E}(\vec{r},t)\\ \vec{B}(\vec{r},t)\end{pmatrix}. \tag{2.7}$$

It can be approximated using the split-operator technique [12,13] with

$$U=\exp\{\Delta t[H^v(\vec{\nabla})+H^m(\vec{\nabla},\vec{r})]\}=U^m_{1/2}U^v_1U^m_{1/2}+O(\Delta t^3), \tag{2.8}$$

where

$$U^v_1\equiv\exp[\Delta tH^v(\vec{\nabla})],$$

$$U^m_{1/2}\equiv\exp[\tfrac{1}{2}\Delta tH^m(\vec{\nabla},\vec{r})]. \tag{2.9}$$

These operators do not commute and this decomposition leads to a local error proportional to Δt^3 for each time step. It should be noted that due to the formal structure of these operators, the first two Maxwell's equations (2.1) and (2.2) are automatically satisfied at all times if the initial fields satisfy them [9].

The operators (2.9) may be computed exactly as shown below. The evaluation for the differential operator $\vec{\nabla}$-dependent part is most convenient in the Fourier space, and for the $\vec{r}$-dependent part in the regular configuration space. We transform the field components into the Fourier space, where (k_x,k_y,k_z) represent spatial frequencies along the x,y,z directions. The field components evolve in the Fourier space as shown below,

$$\begin{aligned}\mathcal{F}\begin{pmatrix}\vec{E}(\vec{r},t+\Delta t)\\ \vec{B}(\vec{r},t+\Delta t)\end{pmatrix}&\cong\mathcal{F}U^m_{1/2}\mathcal{F}^{-1}\mathcal{F}U^v_1\mathcal{F}^{-1}\mathcal{F}U^m_{1/2}\mathcal{F}^{-1}\\ &\quad\times\mathcal{F}\begin{pmatrix}\vec{E}(\vec{r},t)\\ \vec{B}(\vec{r},t)\end{pmatrix}\\ &=\tilde{U}^m_{1/2}\tilde{U}^v_1\tilde{U}^m_{1/2}\mathcal{F}\begin{pmatrix}\vec{E}(\vec{r},t)\\ \vec{B}(\vec{r},t)\end{pmatrix},\end{aligned} \tag{2.10}$$

where $\mathcal{F},\mathcal{F}^{-1}$ denote the Fourier transform and the inverse transform, respectively. The tilde refers to the operators in Fourier space given by

$$\tilde{U}^v_1\equiv\exp[\Delta t\mathcal{F}H^v(\vec{\nabla})\mathcal{F}^{-1}], \tag{2.11}$$

$$\tilde{U}^m_{1/2}\equiv\exp[\tfrac{1}{2}\Delta t\mathcal{F}H^m(\vec{\nabla},\vec{r})\mathcal{F}^{-1}]. \tag{2.12}$$

The operators (2.5) and (2.6) in the Fourier space are diagonalized and the resulting diagonal matrix is easily exponentiated leading to

$$\tilde{U}^v_1=\begin{bmatrix}\mathcal{C} & \mathcal{S}\\ -\mathcal{S} & \mathcal{C}\end{bmatrix}, \tag{2.13}$$

$$\tilde{U}^m_{1/2}=\left(\mathcal{I}+\frac{\Delta t}{2}\mathcal{F}\left\{\frac{c^2}{\epsilon(\vec{r})}-1\right\}\mathcal{F}^{-1}\begin{bmatrix}0 & \mathcal{D}\\ 0 & 0\end{bmatrix}\right), \tag{2.14}$$

where $\mathcal{C}$, $\mathcal{S}$, and $\mathcal{D}$ are 3×3 matrices corresponding to the three field components, and $\mathcal{I}$ is a 6×6 unit matrix. It should be noted that the application of the operator $\tilde{U}^m_{1/2}$ involves going back and forth between the coordinate and the Fourier space. The matrix elements in Eqs. (2.13) and (2.14) are

$$\mathcal{C}=\begin{pmatrix} \dfrac{(k_x^2+k_y^2)(k_x^2+k_z^2)[k_x^2+(k_y^2+k_z^2)\cos k\Delta t]}{k^2(k_x^2k^2+k_y^2k_z^2)} & -\dfrac{k_xk_y(\cos k\Delta t-1)}{k^2} & -\dfrac{k_xk_z(\cos k\Delta t-1)}{k^2} \\ -\dfrac{k_xk_y(\cos k\Delta t-1)}{k^2} & \dfrac{(k_x^2+k_y^2)(k_x^2+k_z^2)[k_y^2+(k_x^2+k_z^2)\cos k\Delta t]}{k^2(k_x^2k^2+k_y^2k_z^2)} & -\dfrac{k_yk_z(\cos k\Delta t-1)}{k^2} \\ -\dfrac{k_xk_z(\cos k\Delta t-1)}{k^2} & -\dfrac{k_yk_z(\cos k\Delta t-1)}{k^2} & \dfrac{k_z^2+(k_x^2+k_y^2)\cos k\Delta t}{k^2} \end{pmatrix}, \tag{2.15}$$

$$\mathcal{S}=\begin{pmatrix} 0 & -\dfrac{ik_z\sin k\Delta t}{k} & \dfrac{ik_y\sin k\Delta t}{k} \\ \dfrac{ik_z\sin k\Delta t}{k} & 0 & -\dfrac{ik_x\sin k\Delta t}{k} \\ -\dfrac{ik_y\sin k\Delta t}{k} & \dfrac{ik_x\sin k\Delta t}{k} & 0 \end{pmatrix}, \tag{2.16}$$

$$\mathcal{D}=\begin{pmatrix} 0 & -ik_z & ik_y \\ ik_z & 0 & -ik_x \\ -ik_y & ik_x & 0 \end{pmatrix}. \tag{2.17}$$

Here $k\equiv\sqrt{k_x^2+k_y^2+k_z^2}$. In vacuum $[\epsilon(\vec{r})\equiv1]$ the operator $\tilde{U}^m_{1/2}$ reduces to the unit operator. The transformation of the field components between coordinate and Fourier space $(x,y,z)\leftrightarrow(k_x,k_y,k_z)$ is performed via efficient fast Fourier transform routines. We next discuss the initial and boundary conditions used to simulate diverse applications.

B. Initial conditions

We specify the initial field distribution and the functional form of $\epsilon(\vec{r})$. We will discuss in this section the variety of initial field distributions, representing a nearly ideal plane wave and a typical laser beam, used in conjunction with the algorithm. We have the flexibility of either launching a pulse localized in space and time or feeding in a continuous wave (cw) field. We describe below the details of these input fields, particularly the cw field, which is achieved without increasing the spatial domain of integration.

1. Input plane-wave field

We have developed a method of efficiently producing a quasimonochromatic wave which is localized in the transverse spatial direction, has a constant amplitude in the longitudinal direction, and any desired pulse length. In principle, a plane wave of the form $\exp(\pm i\vec{k}\cdot\vec{r}-i\omega t)$ is the exact solution of the Maxwell's equations. In practice, there are technical limitations of simulating such a plane-wave cw field with infinite extent in all directions, as this would require an infinite spatial domain of integration. In the transverse directions, we choose a broad spatial extent of the wave front that is contained by a Gaussian profile. It is important to have the field components approaching zero near the boundaries because of the built-in periodicity of the frequency space. This is also known as the wrap-around effect, which results from a large contribution at one boundary being carried over to the opposite boundary. We ensure that even in the longitudinal direction, all the field components are negligible at the boundaries. Usually the physical extent (in the longitudinal direction) of a quasi-cw input field is strongly limited by the spatial extent of the domain of integration. To overcome this limitation, we update the tail end of the field at precise times and spatial locations in our spatial integration domain, such that we can simulate a pulse of any desired length. The choice of these times and location is quite critical, which if not undertaken carefully would result in introducing unwanted frequency components in the input field. We also implement absorbing boundary conditions and discuss the details in Sec. II C. We show below how one can obtain any desired pulse length without increasing the spatial domain of integration.

For simplicity, we discuss the formation of the cw field in a reduced dimensional configuration and freeze the x direction. The procedure described below applies, of course, to three dimensions. Our spatial domain is now $(-L_y,L_y)$ along the y direction and $(-L_z,L_z)$ in the z direction. At time $t=0$, the initial field contains a finite wave located, along the z axis, at $y=0$ and left of the origin. We choose the z direction as the direction of propagation, so the field in vacuum would travel from left to right along the z axis. The initial field is

$$\vec{E}(\vec{r},t=0)=\hat{e}_x E_i(y,z)\exp[ik_{0z}z],$$
$$\vec{B}(\vec{r},t=0)=\hat{e}_y \frac{E_i(y,z)}{c}\exp[ik_{0z}z], \tag{2.18}$$

where k_{0z} is the wave number of the field, and $\hat{e}_x$ and $\hat{e}_y$ are the unit vectors. Here, $E_i(y,z)$ contains the spatial extent along the y direction as well as the finite profile of the field along the z direction. In the z direction, we choose a smooth turn-on and turn-off for the finite wave. This ensures that there are no high-frequency contributions to the Fourier spectra due to a sharp cutoff of the input wave train. The field components are transformed into the Fourier space and evolve in accordance with Eq. (2.10). After a finite-time duration, say τ, the wave travels a distance of $c\tau/n_1$ (c being the speed of light associated with refractive index n_1) from left to right. We now update the tail end of the field after times $\tau=m\Delta t$ in which the field travels a distance $p\Delta z$, where m and p are the smallest possible integers in $m/p=n_1\Delta z/(c\Delta t)$. The advantage is twofold. First, m and p being integers results in the field having moved an integral number of spatial grid points along the z direction, thus minimizing the Gibbs overshoot effect [14]. Second, small values of m and p minimize the expansion of the wave in the transverse y direction, which invariably occurs due to the finite extent of the wave front in the transverse direction. This updating of the tail end of the field is undertaken in the coordinate space and subsequently the field components are transformed back into the Fourier space for further evolution under Eq. (2.10). This process can be applied repeatedly to obtain a wave of a desired longitudinal extent.

2. Input Gaussian beam

To model an incident Gaussian beam propagating in the z direction and polarized in the x direction, the following initial state is used:

$$\vec{E}(\vec{r},t=0)=\frac{\hat{e}_x A e^{-i\phi(z)}}{\sqrt{1+(z-z_i)^2/(z_0-z_i)^2}} \times e^{ik(x^2+y^2)/[2R(z)]}e^{-(x^2+y^2)/w^2(z)} \tag{2.19}$$

and similarly for $\vec{B}$ where for a finite pulse $A\equiv\exp[-(z-z_i)^2/(2z_w^2)]$, which gives the extension z_w of the pulse in the propagation direction, which is centered at $z=z_i$. $R(z),\phi(z),w(z)$ are of the following form:

$$R(z)=(z-z_i)+(z_0-z_i)^2/(z-z_i),$$
$$\phi(z)=\tan^{-1}(z-z_i)/(z_0-z_i), \tag{2.20}$$
$$w(z)=w_0\sqrt{1+(z-z_i)^2/(z_0-z_i)^2},$$

where $w_0^2=\lambda z_0/\pi$. Equation (2.20) shows that the wave front is purely planar at $z=z_i$ as $R\to\infty$, and the pulse waist at $z=z_i$ in the (x,y) direction is w_0 from Eq. (2.20). Along the z direction, the intensity profile is Gaussian (by choice of the function A). As discussed earlier, we can also simulate a quasi-cw field by choosing an appropriate form for A in Eq. (2.19) and proper updating of the field as outlined in Sec. II B 1. For $A=1$, the field in the z direction about the point $z=z_i$ would vary as $\sim 1/z$ such that at $z-z_i=z_0$ the waist of the beam $w(z_0)=w_0\sqrt{2}$. It should be noted that for $A=1$, the field in Eq. (2.19) satisfies exactly the paraxial wave equation which assumes a slowly varying envelope along the propagation direction [15]. For the choice of a Gaussian envelope for A, if the pulse width $z_w\gg\lambda$, the paraxial approximation is still quite valid and the field would be a solution of the paraxial wave equation. While Eqs. (2.18) and (2.19) state the conditions of a field with finite extension at the initial moment, after repeated application of the time-evolution operators the field cannot be contained in the spatial computational domain. Hence, we next discuss the computational boundary conditions imposed in our algorithm that regulate the size of the spatial domain of integration.

C. Computational boundary conditions

We use absorbing boundary conditions to achieve long integration times in a relatively small spatial integration domain. Any field in the region close to the boundary is multiplied by a function which approaches zero smoothly around the boundary and is unity away from it (like the square of the cosine function). This method works sufficiently and does not result in reflections greater than 10^{-5}% from these regions near the boundary. This operation is carried out at the times $m\Delta t$, and the region of variation of this smooth function near the boundary is dictated by the distance traveled by the field in this time. This region is chosen to be larger than $p\Delta i$, for $i=x,y,z$ to ensure that even partial fragments of the field do not contribute to any wrap-around effect along both the transverse and the longitudinal directions. The integers m,p are the same as described in Sec. II B 1. We apply these absorbing boundary conditions in the coordinate space (x,y,z), and then transform the electromagnetic field back into the Fourier domain (k_x,k_y,k_z) for further evolution. In the case of a quasi-cw incident field, the boundary conditions are applied along all but one boundary. This boundary is the one from which the cw field emanates; the formation of the cw field itself replaces any outgoing field in this region by an incoming cw field. We now discuss a few applications of this algorithm.

III. APPLICATIONS

In this section we calculate the spatiotemporal field evolution for three different configurations. We make comparisons of our numerical results for simple geometries for which analytical expressions can be derived to demonstrate the accuracy of the numerical code.

A. Simple interface

We consider first a monochromatic plane wave incident on an air-glass interface and compare the Fresnel coefficients for various incident angles. The geometry of the interface is depicted in Fig. 1 where the air-glass interface is along the $z=y$ plane, with z and y being the horizontal and vertical directions, respectively. The refractive indices for the two media are n_1 for $z<y$ and n_2 for $z\geqslant y$. We also display in the figure the reflected and refracted beams. The refracted beam travels with a velocity c/n_2 and has a wavelength of

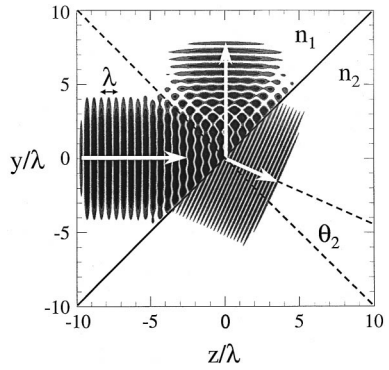

FIG. 1. A plane wave incident on an air-glass ($n_2=2$) interface with $\theta_1=45°$. The arrows denote the incident, reflection, and the refraction direction, which are in agreement with Snell's laws. The refracted field in the glass propagates with a velocity c/n_2 and wavelength λ/n_2, as can be clearly seen by comparing with the reflected beam.

λ/n_2, with $n_2=2$. For the TE mode, the polarization of the incident field is along the x direction. The incident field is given by Eq. (2.18) in our simulations. In the present calculations, 512×512 grid points were sufficient. In order to change the angle of incidence, we merely rotate the interface, keeping the field propagating along the z direction.

The Fresnel coefficient of the transmitted field for the TE modes is given by [16]

$$\frac{E_t}{E_i}=\frac{2n_1\cos\theta_1}{n_1\cos\theta_1+n_2\cos\theta_2}, \tag{3.1}$$

where E_i is the incident wave amplitude and E_t is the amplitude of the transmitted wave. The angle of incidence is θ_1 and the angle of refraction is θ_2. We observed in our time-resolved wave simulation that the resulting angle of refraction θ_2 is in accordance with Snell's law, i.e., $n_1\sin\theta_1=n_2\sin\theta_2$. In Fig. 2, the circles represent the numerical values of the transmission coefficient obtained for a grid with 12 grid points per wavelength, which are in good agreement with the known results of Eq. (3.1), shown as a solid line. As an example of the accuracy, for $\theta_1=24°$ the numerical value obtained was 0.636 03 compared to the analytical result of 0.636 23; an agreement of 99.97% is obtained. This agreement is still quite good for only three grid points per wavelength, where it drops to 98.64%. Similar results were confirmed for the reflected waves as well as the TM modes. We should note that, at least in principle, infinitely large frequencies are associated with the abrupt change of the index of refraction. However, our results demonstrate that errors associated with the sharpness of the interface are quite small.

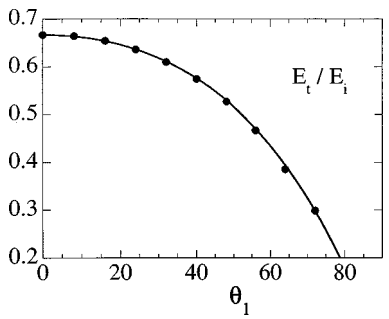

FIG. 2. Comparison of the Fresnel coefficients for an air-glass interface for various incident angles (in degrees). The circles represent the obtained numerical value of the FC for the transmitted field. The corresponding analytical results, Eq. (3.1), are shown by the solid line. ($N_y=N_z=512$, $\Delta t=0.0195\lambda/c$, and $\Delta x=0.0781\lambda$.)

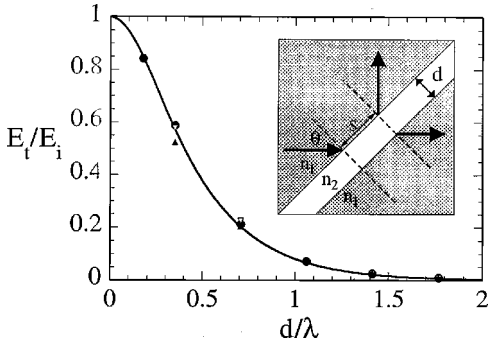

FIG. 3. The amplitude transmission coefficient for the tunneling phenomenon associated with the evanescent field as a function of the barrier thickness d. The analytical result shown by the solid line [from Eq. (3.2)] is compared with numerical values. The inset contains the schematic of the geometry for tunneling of the electromagnetic field from layer I into layer III (both of the refractive index n_1), where layer II with index n_2 acts as a dielectric barrier. [$N_y=N_z=512$ (solid circles), $N_y=N_z=256$ (open triangles), $N_y=N_z=128$ (solid triangles), and $\Delta t=0.0195\lambda/c$.]

B. Tunneling in multilayered media

In this section, we study the propagation of a plane wave in multilayered media, particularly the dynamics of an evanescent wave tunneling through a dielectric barrier. The similarity between tunneling of electrons and the propagation of evanescent waves across a dielectric barrier has been discussed in Refs. [17,18]. The barrier results from a low-dielectric region that is sandwiched between two high-dielectric regions. For an appropriate incident angle θ of the input field from the high-dielectric region, the region of low dielectricity acts like a barrier. The phenomenon of tunneling itself has always attracted a great deal of attention as well as a lot of controversies [19]. There has been no consensus on the issue of the amount of time a photon (in general any particle) spends inside the barrier, but there are other noncontroversial aspects of tunneling such as the transmission/reflection coefficient. We simulate the process of optical tunneling and obtain the transmission coefficient for comparison with the analytical results and leave out the other aspects for future investigation.

The three layers are, as shown in the inset of Fig. 3, the semi-infinite layer I (refractive index n_1), the barrier layer II of thickness d (refractive index n_2), and the semi-infinite layer III (refractive index n_1), and s denotes the Goos-Hänchen shift [16]. An incident plane wave polarized in the x direction (TE mode) and incident on the layer I-II dielectric interface at an angle θ experiences total internal reflection for $\theta>\arcsin(n_2/n_1)$. The amplitude transmission coefficient is given by [20]

$$\frac{E_t}{E_i}=\frac{2k_{1z}K/\sinh(Kd)}{\sqrt{(k_{1z}^2-K^2)^2+4k_{1z}^2K^2\coth^2(Kd)}}, \tag{3.2}$$

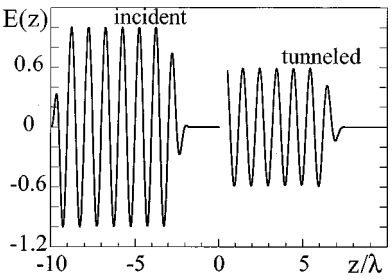

FIG. 4. The turn-on segment of the transmitted field in the multilayer interaction described in Fig. 3. The stretching of the front end in comparison to the input field is shown on the left. Also note the overshoot of the tunneled field before it settles into a steady state. ($N_y = N_z = 512$, $d/\lambda = 0.3535$, and $\Delta t = 0.0195\lambda/c$.)

where $k_{1z} = k_1 \cos\theta$, $k_{1y} = k_1 \sin\theta$, and $K = \sqrt{k_{1y}^2 - k_2^2}$, with k_1 and k_2 being the wave numbers in the region of refractive index n_1 and n_2, respectively. An incident plane-wave (2.18) field propagating along the z direction is incident at the $z = y$ interface (again assuming z and y to be the horizontal and vertical directions, respectively) at an angle $\theta = \pi/4 \sim 0.785$ rad and experiences total internal reflection at the layer I-II interface, as θ is greater than the critical angle of 0.524 rad for the choice of $n_1 = 2$ and $n_2 = 1$. Only a small fraction of the incident field enters the layer II and this evanescent field decays nearly exponentially, with K as the coefficient of extinction, and acts as the source of the field that tunnels through into layer III.

We obtained numerically the amplitude transmission coefficient of the field in the steady-state (cw) limit and find that it matches quite well with the analytical result as shown in Fig. 3. The analytical expression for the transmission coefficient Eq. (3.2) assumes a cw input wave, whereas any realistic field would have an initial turn-on. In our simulation, we have a semi-infinite pulse with a smooth turn-on over two to three optical cycles (such as the square of the cosine function). After an initial transient period, which depends on the thickness of the barrier (layer II), the transmitted field settles into a steady state. For example, at $d/\lambda = 0.177$ the agreement is 99.2% for a 512×512 grid.

Our fully time-resolved study of the tunneling process reveals two interesting features that become apparent at the turn-on of the pulse. First, one observes stretching of the turn-on segment by 4% of the tunneled field in comparison with the incident field, as shown in Fig. 4. The stretching of the pulse is not present in the constant-amplitude cw segment. We also observe a slight difference ($\sim 0.17\%$ in this case) between the positive and negative peak amplitudes of the transmitted electric field. This results in alternating intensity maxima at early times. This feature disappears at later times as the field settles into a steady state.

The second interesting feature is observed at the leading edge of the cw segment. The negative peak (at $z/\lambda = 6.0$) in Fig. 4 is 0.8% larger than the steady-state value. The relative strength of this peak increases with increasing barrier width or equivalently with decreasing wavelength. For obtaining the transmission coefficient in Fig. 3, we used the steady-state average peak value.

C. Light propagation through random media

In this section, we demonstrate the flexibility and power of our numerical approach, wherein we deal with scattering of an incident Gaussian pulse (2.19) on a large collection of scatterers of random shape, sizes, refractive indices, and locations. To be able to simulate with full time resolution the propagation of an electromagnetic radiation pulse through a medium consisting of random scatterers is the main motivation for the development of the simulation code.

As is apparent, there are no analytical solutions for such a complex problem. Most of the current knowledge about the optical properties of highly scattering inhomogeneous random media is based on the transport theory and the diffusion approximation. For a review, see the two books by Ishimaru [21]. These theories do not incorporate any wave character of the field, and diffractive and interference effects such as multiple reflection inside each scatterer cannot be predicted accurately. It has been shown [22,23] that the diffusion approximation can model the light propagation in thick samples, which are thicker than seven times the extinction length due to scattering and absorption of the field. This approximation, however, is incapable of obtaining field distribution near surfaces on the order of the wavelength. One has to resort to numerical simulation to obtain space and time-resolved distributions of the field.

There are, of course, a wide variety of questions that can be raised for this kind of random medium. Is there an effective ''average'' index of refraction that describes its optical response? How do the scattering properties of the medium depend on the distribution of sizes of the scatterers, on their distribution of indices of refraction, and on their density? How does the average penetration depth depend on the material constants? How do the effects of scattering and refraction interplay in the inhomogeneous random media and how does the roughness of the surface affect the quality of the reflected field? The precise relation between miscroscopic and macroscopic properties of random media is still an open question.

A detailed discussion of the exact Maxwell's equation approach in the context of the diffusion approximation—its limitations and regime of validity—will be presented elsewhere. The focus of the present work is the algorithm of the computional method. We will present here a concrete but simple example to illustrate certain near-field effects resulting from such highly scattering media. The physics of these effects will be investigated in future studies.

We model a collection of 400 ellipsoidal dielectric scatterers of random radii (varying from 0.3λ to 0.7λ), having random refractive indices ($1.1 < n < 1.5$) and located randomly in the y-z plane; the system is assumed to have infinite extension in the x direction for simplicity. The features of the incoming electromagnetic pulse such as the frequency, the temporal, and the spatial width along the transverse and longitudinal directions can be easily controlled in our simulation. To model a laser pulse, we use a Gaussian beam of Eq. (2.19) as the initial input field. The parameters (in units of λ) used in our calculation are beam waist $w_0 = 8$. The pulse is centered along the z axis at $z_i = -18$ with a Gaussian profile overlaid along the z direction of width $z_w = 5$.

In Fig. 5, we display four snapshots of the radiation pulse in the z,y plane ($x = 0$) as it enters the inhomogeneous medium with the interface along the $z = y$ plane. The upper left figure shows the contour plot of the intensity defined as E^2

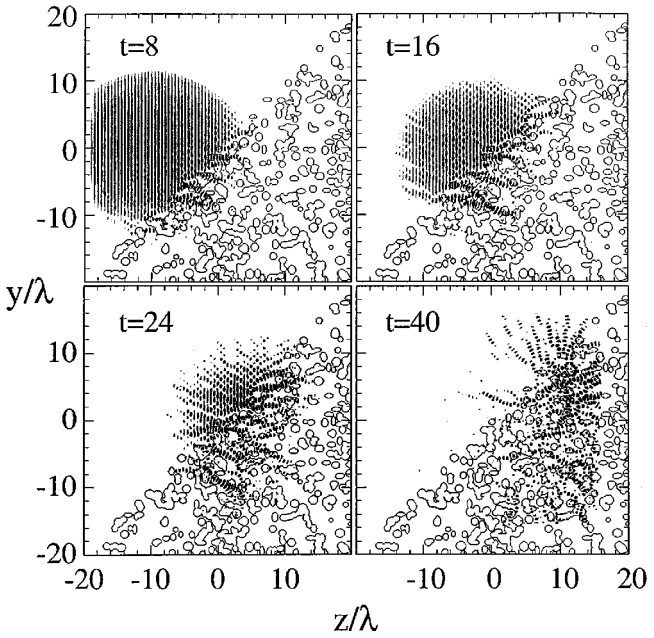

FIG. 5. Contour plots of a laser pulse interacting with a random medium consisting of a large number of dielectric scatterers at times $t=4$, 8, 24, and 40 (in units of λ/c). Note the various near-field effects which are dominantly coherent in nature. ($N_y=N_z=512$, $\Delta t=0.0195\lambda/c$, and $\Delta x=\lambda/12.8$.)

for the incoming laser pulse just as it enters the ''interface'' with the medium at an angle of 45°. The wavelength of $\lambda=1$ and the turn-on segment of the pulse over 5λ is clearly visible in this plot.

The appearance of small ''jets'' that penetrate into the medium is apparent. This feature arises as the scatterers focus part of the incoming wave due to their curvature. Another interesting aspect of the interaction that cannot be described by the transport theory is the interference intensity pattern close to the interface between incoming and partially reflected waves. Some of the outgoing waves are reflected directly at the interface, whereas other waves are diffusively scattered after the interaction with several scatterers inside the medium. This effect leads to a temporal and spatial widening of the reflected beam and corresponding interference effects that appear as dark spots (peaks of intensity maxima).

The lower two figures show the intensity distribution at later times when most of the incoming beam has crossed the interface. In contrast to the simulation with a smooth interface as discussed in Sec. III A, a precise angle for the refracted and reflected beam cannot be defined. The highly diffusive medium acts much more like a large irregularly shaped scatterer such that the reflected intensity is distributed in a cone around the average scattering angle equal to the incoming angle.

Another aspect of the dynamics is the formation of interesting quasistationary intensity patterns inside the medium. If one compares the intensity profiles inside the small square areas $0\leqslant z\leqslant 2$ and $-10\leqslant y\leqslant -8$ for $t=16$ and 24, one sees a very similar pattern that is reminiscent of standing waves between specific scatterers. The pattern may be an indication of coherent backscattering.

IV. CONCLUSION

We presented a numerical algorithm that is capable of producing exact spatio-temporal solutions of the Maxwell equations. The method is easy to program and includes all phase and near-field effects. It may serve as a good tool to test the validity of the Boltzmann theory in random scattering media. As the core part of the program involves the repeated operation of the fast Fourier transformation, the code is easily implemented on parallel supercomputers.

We point out that our approach is quite different from the conventional approach, wherein to solve the Maxwell's equations traditionally requires the expansion onto basis states. The coefficients in this expansion are dictated by careful matching of the scattering states satisfying certain boundary conditions. In contrast, we view Maxwell's equations as a set of differential equations that govern the time evolution of the fields, similar in spirit to the wave-function solutions of the time-dependent Schrödinger or Dirac equation [24].

The proposed algorithm of simulating the interaction of pulses with inhomogeneous random media will face several challenges in the future. A key problem is the restricted spatial domain that is accessible due to finite computer memory. With respect to storage, the method has advantages over the grid methods that are based on finite differences, as the sampling rate can be chosen much smaller and thus fewer grid points are required per wavelength. In a typical three-dimensional calculation, a resolution of about 64 to 512 spatial grid points per spatial direction might not be sufficient to investigate a real material such as a biological tissue. Another question concerns the generality of each simulation. Even though each medium is based on random numbers, it could well be that in order to model a real medium, one needs to average the results of several simulations to get statistically significant data, which are characterized by macroscopic quantities such as the scatter density and do not depend on the details of the random number distributions.

ACKNOWLEDGMENTS

We acknowledge helpful discussions with Dr. T. Foster, Dr. E. Gratton, and Dr. P. Krekora. Numerical and graphical assistance from undergraduate research assistants S.M. Mandel, P.J. Peverly, and R.E. Wagner is deeply appreciated. The project is supported by NSF through Grant No. PHY-9970490 and Research Corporation through Cottrell Science Awards Program. The computations were performed at NCSA.

[1] F. Liu, K.M. Yoo, and R.R. Alfano, Opt. Lett. **18**, 432 (1992).
[2] B.C. Wilson and G. Adam, Med. Phys. **10**, 824 (1983).
[3] S.A. Prahl, M. Keijzer, S.L. Jacques, and A.J. Welch, Dos. Las. Rad. Med. Bio., SPIE series **IS5**, 102 (1989).
[4] K.S. Yee, IEEE Trans. Antennas Propag. **AP-14**, 302 (1966).
[5] A. Taflove and M.E. Brodwin, IEEE Trans. Microwave Theory Tech. **23**, 623 (1970).

[6] K.S. Kunz and R.J. Luebbers, *The FDTD Method for Electromagnetics* (CRC, Boca Raton, 1993).
[7] A. Taflove, *Computational Electrodynamics–The FDTD Method* (Artech House, London, 1995).
[8] See http://www.fdtd.org and K.L. Shlager and J.B. Schneider, IEEE Antennas Propag. Mag. **37**, 39 (1995).
[9] See Chap. 2.1 in Ref. [6].
[10] Q.H. Liu, Microwave Opt. Technol. Lett. **15**, 158 (1997).
[11] P.M. Goorjian and A. Taflove, Opt. Lett. **17**, 180 (1992).
[12] M.D. Feit, J.A. Fleck, Jr., and A. Steiger, J. Comput. Phys. **47**, 412 (1982).
[13] A.D. Bandrauk and H. Shen, J. Chem. Phys. **99**, 1185 (1993).
[14] This overshoot effect occurs due to representation of a sharp edge in the Fourier domain by a finite number of frequency components, a limitation of any discrete (hence finite) Fourier transformation.
[15] P.W. Milonni and J.H. Eberly, *Lasers* (Wiley, New York, 1988).
[16] M. Born and E. Wolf, *Principles of Optics* (Pergamon, Oxford, 1980).
[17] S. Zhu, A.W. Yu, D. Hawey, and R. Roy, Am. J. Phys. **54**, 601 (1986).
[18] Th. Martin and R. Landauer, Phys. Rev. A **45**, 2611 (1992).
[19] E.H. Hauge and J.A. Stovneng, Rev. Mod. Phys. **61**, 917 (1989); R. Landauer and Th. Martin, *ibid.* **66**, 217 (1994).
[20] A. Ghatak and S. Banerjee, Appl. Opt. **28**, 1960 (1989).
[21] A. Ishimaru, *Wave Propagation and Scattering in Random Media* (Academic Press, London, 1978), Vols. I and II.
[22] K.M. Yoo, F. Liu, and R.R. Alfano, Phys. Rev. Lett. **64**, 2647 (1990).
[23] M.C.W. van Rossum and Th.M. Nieuwenhuizen, Rev. Mod. Phys. **71**, 313 (1999).
[24] J.W. Braun, Q. Su, and R. Grobe, Phys. Rev. A **59**, 604 (1999).